Progress In Electromagnetics Research B, Vol. 7, 13–51, 2008

NEW TECHNIQUES TO CONQUER THE IMAGE RESOLUTION ENHANCEMENT PROBLEM

S. E. El-Khamy

Department of Electrical Engineering
Faculty of Engineering
Alexandria University
Alexandria 21544, Egypt

M. M. Hadhoud

Department of Information Technology
Faculty of Computers and Information
Menoufia University
32511, Shebin Elkom, Egypt

M. I. Dessouky, B. M. Salam, and F. E. A. El-Samie

Department of Electronics and Electrical Communications
Faculty of Electronic Engineering
Menoufia University
32952, Menouf, Egypt

Abstract—This paper presents some new techniques for high resolution (HR) image processing and compares between them. The paper focuses on two main topics, image interpolation and image super-resolution. By image interpolation, we mean extracting an HR image from a single Degraded low resolution (LR) image. Polynomial based image interpolation is reviewed. Some new techniques for adaptive image interpolation and inverse image interpolation are presented. The other topic treated in this paper is image super-resolution. By image super resolution, we mean extracting a single HR image either from multiple observations or multiple frames. The paper focuses on the problem of image super resolution using wavelet fusion and presents several super resolution reconstruction algorithms based on the idea of wavelet fusion.

1. INTRODUCTION

In most electronic imaging applications, images with high resolution (HR) are required. HR means that pixel density per unit area in the image is high, and therefore an HR image can offer more details, which are of great importance in many applications. For example, HR images are very helpful in medical applications to facilitate the diagnosis process. HR images are also required in applications such as military imaging because images are captured at remote distances. Satellite space imagery is one of the fields that have a bad need for obtaining HR images from the available captured LR images. In applications such as image compression, LR images are transmitted to save the bandwidth and therefore it is the task of the receiver to obtain HR images from the received LR images. In the processing of old movies, it's also required to obtain HR multi frames from the available LR multi frames. All these applications have motivated the emergence of a new field of image processing called HR image processing.

In recent years, digital imaging cameras for both still images and movies have been widely developed. These cameras are based on charge-coupled devices (CCDs) and CMOS image sensors. Although these imaging cameras have so many advantages compared to classical cameras used previously, they suffer from the problem of limited spatial resolution and their resolution levels and consumer prices are not suitable for future applications. Thus, the limited abilities of digital cameras has been another motivation for the emergence of the HR image processing branch.

The branch of HR image processing concentrates on two main topics, image interpolation and image super resolution. Image interpolation is the process by which a single HR image can be obtained from a single degraded LR one [1–17], while super-resolution reconstruction of images aims at obtaining a single HR image either from several degraded still images or from several degraded multiframes [18–33]. This paper introduces a group of image interpolation and image super-resolution algorithms and some comparisons between them.

2. SINGLE CHANNEL LR IMAGE DEGRADATION MODEL

In the imaging process, when a scene is imaged by an HR imaging device, the captured HR image can be named $f(n_1, n_2)$ where $n_1,\ n_2 = 0, 1, 2, \ldots, N-1$. If the same scene is imaged by an LR imaging device, the resulting image can be named $g(m_1, m_2)$ where $m_1,\ m_2 =$

$0, 1, 2, \ldots, M-1$. Here $M = N/R$, where R is the ratio between the sampling rates of $f(n_1, n_2)$ and $g(m_1, m_2)$. The relationship between the LR image and the HR image, assuming no blurring, can be represented by the following mathematical model [9–12]:

$$\boldsymbol{g} = \boldsymbol{D}\boldsymbol{f} + \boldsymbol{v} \tag{1}$$

where $\boldsymbol{f}, \boldsymbol{g}$ and $\boldsymbol{v}$ are lexicographically ordered vectors of the unknown HR image, the measured LR image and additive noise values, respectively. The $\boldsymbol{f}$ vector is of size $N^2 \times 1$ and the vectors $\boldsymbol{g}$ and $\boldsymbol{v}$ are of size $M^2 \times 1$. The matrix $\boldsymbol{D}$ is of size $M^2 \times N^2$. The matrix $\boldsymbol{D}$ represents the filtering and down sampling process, which transforms the HR image to the LR image. Under separability assumption, the model of filtering and down sampling processes which transforms the $N \times N$ HR image to the $M \times M$ LR image is shown in Fig. 1. Here $M = N/2$.

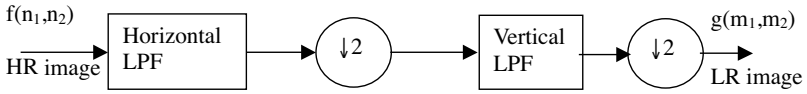

Figure 1. Down sampling process from the $N \times N$ HR image to the $N/2 \times N/2$ LR image.

3. IMAGE INTERPOLATION

The process of image interpolation aims at estimating intermediate pixels between the known pixel values in the available LR image. The image interpolation process can be considered as an image synthesis operation. This process is performed on a one dimensional basis; row by row and then column by column. If we have a discrete sequence $f(x_k)$ of length N as shown in Fig. 2a and this sequence is filtered and down sampled by 2, we get another sequence $g(x_n)$ of length $N/2$ as shown in Fig. 2b. The interpolation process aims at estimating a sequence $l(x_k)$ of length N as shown in Fig. 2c, which is as close as possible to the original discrete sequence $f(x_k)$.

3.1. Linear Space Invariant Image Interpolation

For equally spaced 1-D sampled data, $g(x_n)$, many interpolation functions can be used. The value of the sample to be estimated, $l(x_{k+1})$, can, in general, be written in the form [1–12]:

$$l(x_{k+1}) = \sum_{n=-\infty}^{\infty} c_n \beta(x_{k+1} - x_n) \tag{2}$$

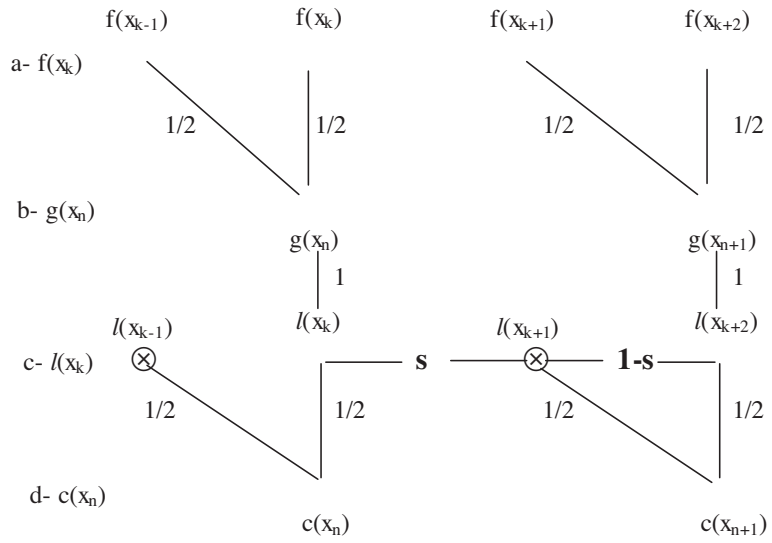

Figure 2. Signal down sampling and interpolation.
a- Original data sequence.
b- Down sampled version of the original data sequence.
c- Interpolated data sequence.
d- Down sampled version of the interpolated data sequence.

where $\beta(x)$ is the interpolation basis function.

From the classical Sampling theory, if $g(x_n)$ is band limited to $(-\pi, \pi)$, then [1–12]:

$$l(x_{k+1}) = \sum_{n=-\infty}^{\infty} g(x_n) \text{sinc}\,(x_{k+1} - x_n) \tag{3}$$

This is known as ideal interpolation. From the numerical computations point of view, the ideal interpolation formula is not practical due to the slow rate of decay of the interpolation kernel $\text{sinc}\,(x)$. So, approximations such as nearest-neighbor, bilinear, B-Spline, Key's (bicubic) and o-Moms basis functions are used as alternative basis functions [1–12].

Thus, Eq. (2) can be implemented on a finite neighborhood rather than carrying out an infinite summation and the coefficients c_n need to be estimated [1–12]. The choice of the basis function $\beta(x)$ can save the step of estimating the coefficients c_n if it is chosen to be an interpolating basis function such as the bilinear and bicubic basis functions.

3.1.1. Nearest-Neighbor Interpolation

Nearest-neighbor interpolation is the simplest interpolation scheme. The basis function associated with nearest-neighbor interpolation is given by [1–12]:

$$\beta^0(x) = \begin{cases} 0 & x < -1/2 \\ 1 & -1/2 \le x \le 1/2 \\ 0 & 1/2 \le x \end{cases} \tag{4}$$

This scheme of interpolation is merely a pixel repetition process and the basis function is interpolating.

3.1.2. Bilinear Interpolation

The bilinear interpolation enjoys a large popularity due to its simplicity of implementation. The basis function used in bilinear interpolation is interpolating and it's given by [1–12]:

$$\beta^1(x) = \begin{cases} 1 - |x| & |x| < 1 \\ 0 & 1 \le |x| \end{cases} \tag{5}$$

As shown in Fig. 2, we define the distance between x_{k+1} and x_n and between x_{k+1} and x_{n+1} as [13–17]:

$$s = x_{k+1} - x_n, \qquad 1 - s = x_{n+1} - x_{k+1} \tag{6}$$

Thus, Eq. (2) can be written as follows [1–12]:

$$l(x_{k+1}) = (1 - s)g(x_n) + sg(x_{n+1}) \tag{7}$$

3.1.3. B-Spline Interpolation

There is a whole family of interpolation basis functions called B-Splines. These functions are piecewise polynomials of degree n. The basis function $\beta^n(x)$ represents the central B-Spline of degree n which is given by [1–12]:

$$\beta^n(x) = \underbrace{\beta^0 * \beta^0 * \cdots * \beta^0(x)}_{(n+1) \text{ times}} \tag{8}$$

From the family of polynomial splines, cubic spline tend to be the most popular in so many applications. The closed form approximation of

the cubic spline basis function is given by [1–12]:

$$\beta^3(x) = \begin{cases} \frac{2}{3} - |x|^2 + \frac{|x|^3}{2} & 0 \le |x| < 1 \\ \frac{(2-|x|)^3}{6} & 1 \le |x| < 2 \\ 0 & 2 \le |x| \end{cases} \tag{9}$$

The cubic spline interpolation formula is given by:

$$\begin{aligned} l(x_{k+1}) \;=\; & c(x_{n-1})[(3+s)^3 - 4(2+s)^3 + 6(1+s)^3 - 4s^3]/6 \\ & + c(x_n)[(2+s)^3 - 4(1+s)^3 + 6s^3]/6 \\ & + c(x_{n+1})[(1+s)^3 - 4s^3]/6 + c(x_{n+2})s^3/6 \end{aligned} \tag{10}$$

B-spline basis functions are non-interpolating and thus, the coefficients in Eq. (2) need to be estimated prior to the interpolation process. This estimation process can be implemented using a digital filtering approach [1–12].

3.1.4. Bicubic Interpolation

Another method which is significantly effective in signal interpolation is the bicubic one. The bicubic interpolation basis function is interpolating and can be expressed in the following form [8, 11]:

$$\beta(x) = \begin{cases} (\alpha+2)|x|^3 - (\alpha+3)|x|^2 + 1 & 0 \le |x| \le 1 \\ \alpha|x|^3 - 5\alpha|x|^2 + 8\alpha|x| - 4\alpha & 1 < |x| \le 2 \end{cases} \tag{11}$$

Thus, the general bicubic interpolation formula is given by [8, 11]:

$$\begin{aligned} l(x_{k+1}) = {} & g(x_{n-1})[\alpha s^3 - 2\alpha s^2 + \alpha s] + g(x_n)[(\alpha+2)s^3 - (3+\alpha)s^2 + 1] \\ & + g(x_{n+1})[-(\alpha+2)s^3 + (2\alpha+3)s^2 - \alpha s] + g(x_{n+2})[-\alpha s^3 + \alpha s^2] \end{aligned} \tag{12}$$

where α is an optimization parameter. It may be adaptive from point to point depending on the signal local activity levels.

3.1.5. O-Moms Interpolation

O-Moms are the family of basis functions that enjoy Maximal Order and Minimal Support. Any of these basis functions can be expressed

as the weighted sum of a B-Spline and its derivatives [5, 6]. For cubic o-Moms image interpolation , the basis function is given by [5, 6]:

$$o-Moms^3(x)=\begin{cases}\frac{1}{2}|x|^3-|x|^2+\frac{1}{14}|x|+\frac{13}{21}, & 0\le|x|\le 1\\ \frac{-1}{6}|x|^3+|x|^2+\frac{85}{42}|x|+\frac{29}{21}, & 1<|x|\le 2\\ 0, & 2\le|x|\end{cases} \tag{13}$$

The o-Moms basis functions are non-interpolating and thus the coefficients in Eq. (2) need to be estimated. This estimation process can be implemented using the same digital filtering approach as in B-Spline image interpolation [5, 6].

3.2. Adaptive Image Interpolation (The Warped Distance Approach)

The idea of warped distance can be used in any of the techniques mentioned in Section 2 to improve their performance. This idea is based on modifying the distance s and using a new distance s' based on the homogeneity or inhomogeneity in the neighborhood of each estimated pixel. The warped distance s' can be estimated using the following relation [9]:

$$s'=s-\tau A_n s(s-1) \tag{14}$$

where A_n refers to the asymmetry of the data in the neighborhood of x and it is defined as [9]:

$$A_n=\frac{|g(x_{n+1})-g(x_{n-1})|-|g(x_{n+2})-g(x_n)|}{L-1} \tag{15}$$

where $L=256$ for 8 bit pixels. The scaling factor L is to keep A_n in the range of -1 to 1.

The parameter τ controls the intensity of warping to avoid blurring of edges in the interpolation process.

3.3. Adaptive Image Interpolation Based on Local Activity Levels

Instead of using the traditional image interpolation techniques mentioned above, a new approach is suggested in this section. This approach depends on weighting the values of the pixels incorporated into the image interpolation process by space variant adaptive weights. The distance s is kept fixed [10].

Adaptive Bilinear

$$l(x_{k+1}) = a_0(1-s)g(x_n) + a_1 s g(x_{n+1}) \tag{16}$$

where,

$$a_0 = 1 - \lambda A_n, \qquad a_1 = 1 + \lambda A_n \tag{17}$$

Adaptive Bicubic

$$\begin{aligned} l(x_{k+1}) \;=\; & a_{-1}g(x_{n-1})[\alpha s^3 - 2\alpha s^2 + \alpha s] \\ & + a_0 g(x_n)[(\alpha+2)s^3 - (3+\alpha)s^2 + 1] \\ & + a_1 g(x_{n+1})[-(\alpha+2)s^3 + (2\alpha+3)s^2 - \alpha s] \\ & + a_2 g(x_{n+2})[-\alpha s^3 + \alpha s^2] \end{aligned} \tag{18}$$

Adaptive Cubic Spline

$$\begin{aligned} l(x_{k+1}) \;=\; & a_{-1}c(x_{n-1})[(3+s)^3 - 4(2+s)^3 + 6(1+s)^3 - 4s^3]/6 \\ & + a_0 c(x_n)[(2+s)^3 - 4(1+s)^3 + 6s^3]/6 \\ & + a_1 c(x_{n+1})[(1+s)^3 - 4s^3]/6 + a_2 c(x_{n+2})s^3/6 \end{aligned} \tag{19}$$

where in (18) and (19),

$$a_{-1} = a_0 = 1 - \lambda A_n, \qquad a_1 = a_2 = 1 + \lambda A_n \tag{20}$$

and λ is a constant which controls the intensity of weighting used for neighboring pixels. Thus, the weighting coefficients are updated at each pixel depending on the asymmetry A_n at this pixel. We note the following special cases:

i- For homogeneous regions, the value of A_n tends to zero which leads to $a_{-1} = a_0 = a_1 = a_2 = 1$. This is equivalent to the traditional image interpolation process.

ii- For positive values of A_n, which means that there is an edge that is more homogeneous on the right side, the weights of the pixels on the right side (a_1 and a_2) are increased and the weights of the pixels on the left side (a_{-1} and a_0) are decreased. This is expected to yield images with better visual quality.

iii- For negative values of A_n, a_{-1} and a_0 are increased and a_1 and a_2 are decreased and the same effect is obtained.

The proposed adaptive weighting technique can also be applied with warped distance image interpolation in all the methods mentioned above. This is clear in Fig. 3 and Table 1 but the enhancement at each pixel position is minimal as shown in Fig. 4. Thus, there is a need for a new adaptive algorithm that is able to give a better performance.

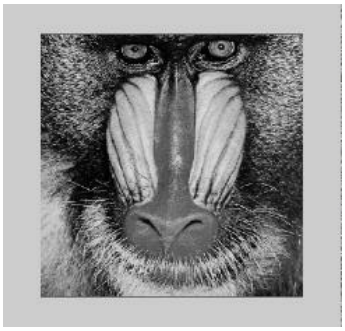

(a) Original Mandrill image

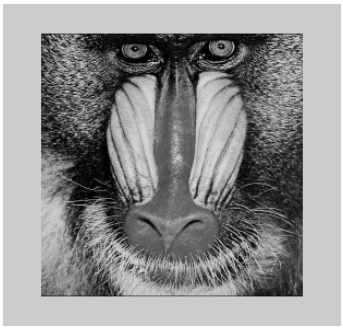

(b) LR Mandrill image.

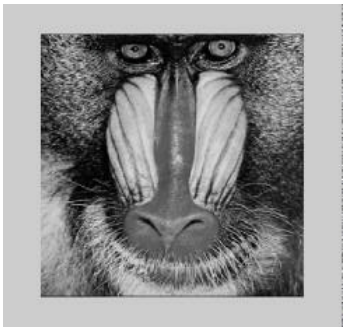

(c) Bicubic Interpolation (no warping). MSE=826.7

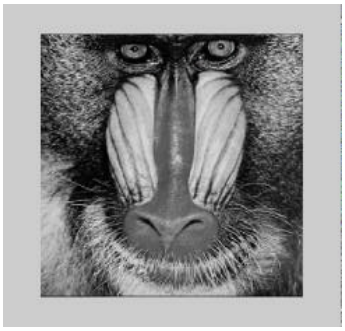

(d) Bicubic interpolation with warping . MSE=807.4

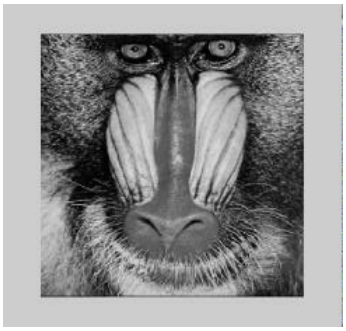

(e) Adaptive Image Interpolation (no warping) MSE=791

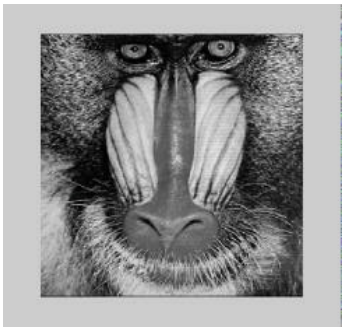

(f) Adaptive image interpolation with warping. MSE=786.4

Figure 3. Simple adaptive interpolation results.

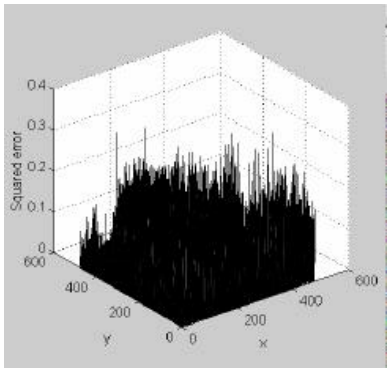

(a) Squared error for bicubic image interpolation

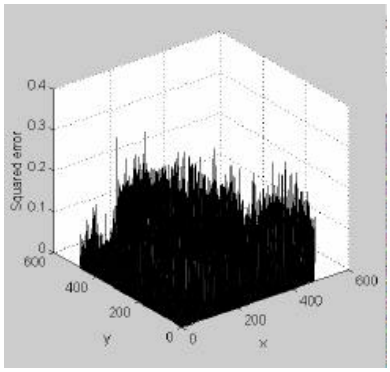

(b) Squared error for adaptive bicubic image interpolation

Figure 4. Squared error at each pixel for the interpolated Mandrill image.

Table 1. MSE for interpolation of the LR Mandrill image using the simple adaptive algorithm.

	Interpolation with no warping	Warped distance Interpolation	Adaptive Weighted interpolation	Adaptive weighted Interpolation with warping
Bilinear	845.09	830.72	808.26	805.72
Bicubic	826.7	807.4	791	786.4
Cubic -spline	855.5	846.23	819.96	816.84

3.4. Space Varying PBP Image Interpolation

Equations (7) and (10) have a single controlling parameter s while Eq. (12) has two controlling parameters s and α which can be optimized to give the best interpolation results. The adaptation can be made pixel by pixel (PBP) depending on the neighboring pixel values [17]. Suppose we have a discrete sequence $f(x_k)$ of length N as illustrated in Fig. 2a. Applying the process of filtering and down sampling on this sequence, we get a sequence $g(x_k)$ of length $N/2$ as given in Fig. 2b. If we apply a polynomial based interpolation process on the resulting sequence $g(x_n)$, we will get a sequence $l(x_k)$ of length N which is required to be as close as possible to $f(x_k)$. This requires the

minimization of the mean squared error (MSE) between the estimated sequence and the original sequence. The minimization of the MSE can be performed by the minimization of the squared error between each estimated sample and its original value.

If the sequence $g(x_n)$ is interpolated using bilinear interpolation to give $l(x_k)$, the squared estimation error between the estimated sample $l(x_{k+1})$ and the original sample $f(x_{k+1})$ is given by [11, 12]:

$$E = [f(x_{k+1}) - l(x_{k+1})]^2 \tag{21}$$

Substituting for $l(x_{k+1})$ from Eq. (7), we get:

$$E = [f(x_{k+1}) - (1-s)g(x_n) - sg(x_{k+1})]^2 \tag{22}$$

But from Fig. 2, we have the following relations:

$$g(x_n) = \frac{1}{2}[f(x_k) + f(x_{k-1})] \tag{23}$$

$$g(x_{n+1}) = \frac{1}{2}[f(x_{k+2}) + f(x_{k+1})] \tag{24}$$

Substituting for $g(x_n)$ and $g(x_{n+1})$ into Eq. (21), we get [12]:

$$E = \left[f(x_{k+1}) - \frac{(1-s)}{2}[f(x_k) + f(x_{k-1})] - \frac{s}{2}f(x_{k+2}) + f(x_{k+1})\right]^2 \tag{25}$$

All sample values are considered constants and E is a function of s only.

Differentiating Eq. (25) with respect to s and equating to zero gives [12]:

$$s_{opt} = \frac{f(x_{k+1}) - g(x_n)}{g(x_{n+1}) - g(x_n)} \tag{26}$$

Thus, at s_{opt}, there is a minimum squared error between the estimated sample $l(x_{k+1})$ and the original sample $f(x_{k+1})$ [12]. The same treatment is possible for all other interpolation methods [12].

It is noted that the sequence $g(x_n)$ is available but the sequence $f(x_k)$ is unavailable. Thus, one cannot directly determine s_{opt} for the above mentioned four cases. To solve this problem, we apply a down sampling operation on the sequence $l(x_k)$ to get a sequence $q(x_n)$ of length $N/2$ as illustrated in Fig. 2d. The squared estimation error between $q(x_{n+1})$ and $g(x_{n+1})$ is given by:

$$E^* = [g(x_{n+1}) - q(x_{n+1})]^2 \tag{27}$$

From Fig. 2, we have:

$$l(x_{k+2}) = g(x_{n+1}) \tag{28}$$

and

$$q(x_{n+1}) = \frac{1}{2}[l(x_{k+1}) + l(x_{k+2})] \tag{29}$$

Substituting from Eqs. (24), (28) and (29) into Eq. (27), we get:

$$E^* = \frac{1}{4}\left[[f(x_{k+1}) - l(x_{k+1})] + \frac{1}{2}[f(x_{k+2}) - f(x_{k+1})]\right]^2 \tag{30}$$

Substituting from Eq. (21) into Eq. (30), we get [12]:

$$E^* = \frac{1}{4}\left[\sqrt{E} + K^2\right] \tag{31}$$

where

$$K = \frac{1}{2}[f(x_{k+2}) - f(x_{k+1})] \tag{32}$$

It is clear that K is a constant with respect to s or with respect to s and α for the bicubic case. For the case of edge interpolation, which is the case of our greatest interest, the side containing $f(x_{k+1})$ and $f(x_{k+2})$ is homogeneous and the side containing $f(x_{k-1})$ and $f(x_k)$ is also homogeneous. This means that the values of $f(x_{k+1})$ and $f(x_{k+2})$ are close to each other and the values of $f(x_{k-1})$ and $f(x_k)$ are also close to each other. Thus, the value of K is small and therefore, the value of s_{opt} which minimizes E leads to the minimization of E^* regardless of the sign of K. Since E is minimum at s_{opt}, then E^* will be minimum at the same value of s_{opt}. For flat areas, the constant K is approximately equal to zero and $E^* \cong E/4$.

From Eq. (31), we can deduce the following equation [11, 12]:

$$E^*_{\min} = \frac{1}{4}\left[\sqrt{E_{\min}} + K\right]^2 \tag{33}$$

To evaluate the value of s_{opt} for the cases of bilinear and cubic Spline interpolation, we follow an iterative manner as follows [12]:

$$s_{i+1} = s_i - \eta_0 \frac{dE^*}{ds}(s_i) \tag{34}$$

where η_0 is the convergence parameter and $s_0 = 1/2$.

In this iterative algorithm, it is required to calculate $\frac{dE^*}{ds}$.

From Eq. (27), we get:

$$\frac{dE^*}{ds} = -2[g(x_{n+1}) - q(x_{n+1})]\frac{dq(x_{n+1})}{ds} \tag{35}$$

Substituting from Eq. (29) into Eq. (35), we get:

$$\frac{dE^*}{ds} = -\left[g(x_{n+1}) - \frac{1}{2}[l(x_{k+1}) + l(x_{k+2})]\right]\frac{dl(x_{k+1})}{ds} \tag{36}$$

The term $\frac{dl(x_{k+1})}{ds}$ is calculated for each interpolation formula as follows:

i- Bilinear [12]:

$$\frac{dl(x_{k+1})}{ds} = -g(x_n) + g(x_{n+1}) \tag{37}$$

ii- Cubic spline [12]:

$$\begin{aligned}\frac{dl(x_{k+1})}{ds} &= c(x_{n-1})[3(3+s)^2 - 12(2+s)^2 + 18(1+s)^2 - 12s^2]/6 \\ &\quad +c(x_n)[3(2+s)^2 - 12(1+s)^2 + 18s^2]/6 \\ &\quad +c(x_{n+1})[3(1+s)^2 - 12s^2]/6 + c(x_{n+2})s^2/2\end{aligned} \tag{38}$$

For the case of bicubic interpolation, we have two controlling parameters s and α. If the sequence $g(x_n)$ is interpolated using the bicubic interpolation formula, then using Eq. (21), the squared estimation error between $l(x_{k+1})$ and the original sample $f(x_{k+1})$ is given by [11]:

$$\begin{aligned}E &= [f(x_{k+1}) - l(x_{k+1})]^2 \\ &= [f(x_{k+1}) - g(x_{n-1})[\alpha s^3 - 2\alpha s^2 + \alpha s] \\ &\quad -g(x_n)[(\alpha+2)s^3 - (3+\alpha)s^2 + 1] \\ &\quad -g(x_{n+1})[-(\alpha+2)s^3+(2\alpha+3)s^2-\alpha s]-g(x_{n+2})[-\alpha s^3+\alpha s^2]]^2\end{aligned} \tag{39}$$

It is required to find the values of s_{opt} and α_{opt} that minimize the value of E in Eq. (39).

The error function E^* is a function of the two parameters s and α. Thus, the minimization of E^* can be performed by equating the gradient of E^* to zero [11].

$$\nabla E^*(s,\alpha) = \begin{bmatrix} \dfrac{\partial E^*(s,\alpha)}{\partial s} \\ \dfrac{\partial E^*(s,\alpha)}{\partial \alpha} \end{bmatrix} = 0 \tag{40}$$

The values of s_{opt} and α_{opt} can be iteratively estimated as follows [11]:

$$\begin{bmatrix} s_{i+1} \\ \alpha_{i+1} \end{bmatrix} = \begin{bmatrix} s_i \\ \alpha_i \end{bmatrix} - \eta_0 \nabla E^*(s_i, \alpha_i) \tag{41}$$

where η_0 is the convergence parameter and $s_0 = 1/2$ and $\alpha_0 = -1/2$.

If α is fixed at $-1/2$ and the optimization is carried out with respect to s only, Eq. (41) is simplified to the form [11]:

$$s_{i+1} = s_i - \eta_0 \frac{dE^*}{ds}(s_i) \tag{42}$$

If s is fixed at $1/2$ and the optimization is carried out with respect to α only, Eq. (41) is simplified to the form [11]:

$$\alpha_{i+1} = \alpha_i - \eta_0 \frac{dE^*}{d\alpha}(\alpha_i) \tag{43}$$

The values of $\frac{\partial E^*}{\partial s}$ and $\frac{\partial E^*}{\partial \alpha}$ are calculated from Eq. (27) as follows [11]:

$$\frac{\partial E^*}{\partial s} = -2[g(x_{n+1}) - q(x_{n+1})]\frac{\partial q(x_{n+1})}{\partial s} \tag{44}$$

$$\frac{\partial E^*}{\partial \alpha} = -2[g(x_{n+1}) - q(x_{n+1})]\frac{\partial q(x_{n+1})}{\partial \alpha} \tag{45}$$

Substituting from Eqs. (18) and (28) into Eq. (29), we get [11]:

$$\begin{aligned} q(x_{n+1}) = {} & \frac{1}{2}g(x_{n-1})[\alpha s^3 - 2\alpha s^2 + \alpha s] + \frac{1}{2}g(x_n)[(\alpha+2)s^3 - (3+\alpha)s^2 + 1] \\ & + \frac{1}{2}g(x_{n+1})[-(\alpha+2)^3 + (2\alpha+3)s^2 - \alpha s + 1] + \frac{1}{2}g(x_{n+2})[-\alpha s^3 + \alpha s^2] \end{aligned} \tag{46}$$

Using Eq. (46), we get [11]:

$$\begin{aligned} \frac{\partial q(x_{n+1})}{\partial s} = {} & \frac{1}{2}g(x_{n-1})[3\alpha s^3 - 4\alpha s + \alpha] + \frac{1}{2}g(x_n)[3(\alpha+2)s^3 - 2(3+\alpha)s] \\ & + \frac{1}{2}g(x_{n+1})[-3(\alpha+2)s^2 + 2(2\alpha+3)s - \alpha] + \frac{1}{2}g(x_{n+2})[-3\alpha s^2 + 2\alpha s] \end{aligned} \tag{47}$$

$$\begin{aligned} \frac{\partial q(x_{n+1})}{\partial \alpha} = {} & \frac{1}{2}g(x_{n-1})[s^3 - 2s^2 + s] + \frac{1}{2}g(x_n)[s^3 - s^2] \\ & + \frac{1}{2}g(x_{n+1})[-s^3 + 2s^2 - s] + \frac{1}{2}g(x_{n+2})[-s^3 + s^2] \end{aligned} \tag{48}$$

(a) Original image

(b) LR image
SNR=20 dB.

Figure 5. Lenna image.

(a) Bilinear interpolation

(b) Bilinear with warped distance

(c) Adaptive Bilinear

Figure 6. Bilinear interpolation ($SNR = 20\,\mathrm{dB}$).

This iterative algorithm is used for the estimation of each pixel in the interpolation process. The optimization process of the bicubic image interpolation formula can be performed either with respect to a single parameter (s or α) or with respect to both parameters.

Several experiments have been carried out to test the suggested adaptive image interpolation algorithm on the Lenna image given in Fig. 5. The results given in Figs. 6 to 9 reveal that the suggested adaptive image interpolation algorithm is better in performance than the traditional algorithms.

Other experiments on the above mentioned algorithms with different images have also been carried out and the results are given in Tables 2 to 4. These results show that the suggested adaptive algorithm gives better results for different images with different signal to noise ratios.

3.5. Inverse Image Interpolation

This section focuses on solving the image interpolation problem of noisy images as an inverse problem, taking into consideration the mathematical model which relates the available noisy LR image to the

(a) Cubic Spline

(b) Cubic Spline with warped distance

(c) Adaptive Cubic Spline

Figure 7. Cubic Spline interpolation ($SNR = 20\,\mathrm{dB}$).

(a) Bicubic interpolation

(b) Bicubic with warped distance

(c) Adaptive Bicubic

Figure 8. Bicubic interpolation ($SNR = 20\,\mathrm{dB}$).

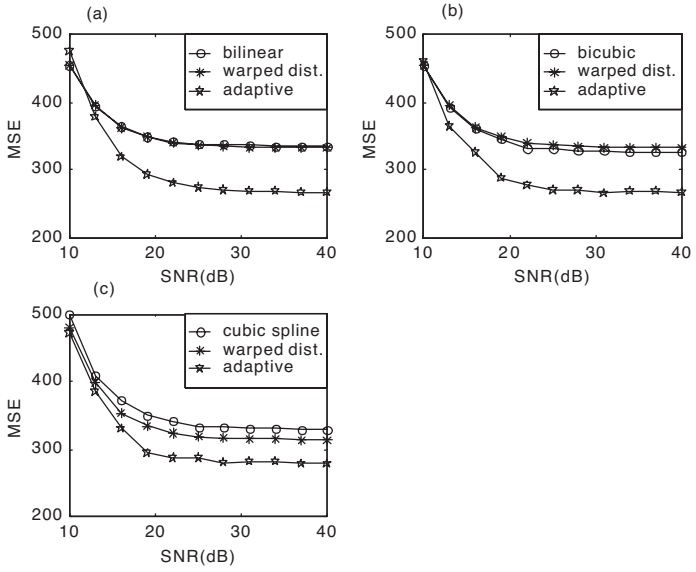

Figure 9. MSE vs. SNR for Lenna image interpolation.

Table 2. MSE for bilinear interpolation of different images.

Image	Bilinear	Bilinear (warped distance)	Adaptive Bilinear	Bilinear	Bilinear (warped distance)	Adaptive Bilinear
	Noise Free interpolation			SNR=20 dB		
Cameraman	253	237	197	274	257	234
Lenna	336	333	269	347	346	289
Mandrill	834	800	685	852	820	716
Building	1201	1170	965	1213	1183	983
TestPat1	333	345	277	359	370	324

Table 3. MSE for bicubic interpolation of different images.

Image	Bicubic	Bicubic (warped distance)	Adaptive Bicubic	Bicubic	Bicubic (warped distance)	Adaptive Bicubic
	Noise Free interpolation			SNR=20 dB		
Cameraman	243	223	194	267	249	231
Lenna	327	324	270	341	339	289
Mandrill	818	772	690	840	798	722
Building	1207	1164	966	1223	1176	979
TestPat1	304	319	263	335	348	308

Table 4. MSE for cubic spline interpolation of different images.

Image	Cubic Spline	Cubic Spline (warped distance)	Adaptive Cubic Spline	Cubic Spline	Cubic Spline (warped distance)	Adaptive Cubic Spline
	Noise Free interpolation			SNR=20 dB		
Cameraman	251	215	215	281	255	255
Lenna	329	314	273	330	347	295
Mandrill	842	814	731	870	840	762
Building	1267	1240	1074	1281	1258	1090
TestPat1	298	267	267	334	310	310

required HR image. Three fast inverse image interpolation approaches are presented and compared from the MSE and computational complexity points of view. These approaches are the Linear Minimum Mean Square Error (LMMSE) approach, the maximum entropy approach and the regularized approach.

3.5.1. Linear Minimum Mean Square Error (LMMSE) Image Interpolation

The LMMSE criterion requires the MSE of estimation to be minimum over the entire ensemble of all possible estimates of the image. The optimization problem here is given by [15, 17]:

$$\min_{\hat{\boldsymbol{f}}} E[\boldsymbol{e}^t\boldsymbol{e}] = E[Tr(\boldsymbol{e}\boldsymbol{e}^t)] \tag{49}$$

with

$$\boldsymbol{e} = \boldsymbol{f} - \hat{\boldsymbol{f}} \tag{50}$$

where $\hat{\boldsymbol{f}}$ is the estimate of the HR image $\boldsymbol{f}$, which is captured assuming that an HR camera is used. Solving this optimization problem based on Eq. (1) leads to the following solution [15, 17]:

$$\hat{\boldsymbol{f}} = \boldsymbol{R}_f\boldsymbol{D}^t(\boldsymbol{D}\boldsymbol{R}_f\boldsymbol{D}^t + \boldsymbol{R}_v)^{-1}\boldsymbol{g} \tag{51}$$

In this solution, the noise is assumed to be independent on the image such that:

$$E[\boldsymbol{f}\boldsymbol{v}^t] = E[\boldsymbol{v}^t\boldsymbol{f}] = [\boldsymbol{0}] \tag{52}$$

The autocorrelation matrices given in Eq. (51) are defined as follows [15, 17]:

$$\boldsymbol{R}_f = E[\boldsymbol{f}\boldsymbol{f}^t] \tag{53}$$

and

$$\boldsymbol{R}_v = E[\boldsymbol{v}\boldsymbol{v}^t] \tag{54}$$

The matrix $\boldsymbol{R}_v$ is a diagonal matrix whose main diagonal elements are equal to the noise variance of the noisy LR image.

The matrix $\boldsymbol{R}_f$ can be approximated by a block diagonal matrix in the form [15, 17]:

$$\boldsymbol{R}_f = \begin{bmatrix} \boldsymbol{R}_{00} & \boldsymbol{0} & \cdots & \boldsymbol{0} \\ \boldsymbol{0} & \boldsymbol{R}_{11} & \ddots & \vdots \\ \vdots & \ddots & \ddots & \boldsymbol{0} \\ \boldsymbol{0} & \cdots & \boldsymbol{0} & \boldsymbol{R}_{N-1N-1} \end{bmatrix} \tag{55}$$

If the samples of each column are assumed uncorrelated except for each pixel with itself, each matrix $\boldsymbol{R}_{ii}$ can be approximated by a diagonal matrix for $i = 0, 1, \ldots, N-1$.

The main diagonal elements of the matrix $\boldsymbol{R}_{ii}$ can be approximated from the polynomial based interpolated images.

For an image $f'(n_1, n_2)$, the autocorrelation at the spatial location (n_1, n_2) can be estimated from the following relation [15, 17]:

$$R_f(n_1, n_2) \cong \frac{1}{w^2} \sum_{k=1}^{w} \sum_{l=1}^{w} f'(k, l) f'(n_1 + k, n_2 + l) \tag{56}$$

where w is an arbitrary window length for the autocorrelation estimation.

The image $f'(n_1, n_2)$ may be taken as the bilinear, bicubic or cubic spline interpolated image. Thus, the matrix $\boldsymbol{R}_f$ can be approximated by a diagonal sparse matrix.

3.5.2. Maximum Entropy Image Interpolation

If the samples of the lexicographically ordered image are normalized to a maximum of 1, these samples can be considered as probabilities. Thus, the entropy of the sampled image is defined as follows [17]:

$$E = -\sum_{i=1}^{N^2} f_i \log_2(f_i) \tag{57}$$

where E is the entropy and f_i is the sampled signal.

This equation can be written in the vector form as follows [17]:

$$E = -\boldsymbol{f}^t \log_2(\boldsymbol{f}) \tag{58}$$

For image interpolation, to maximize the entropy subject to the constraint that $\|\boldsymbol{g} - \boldsymbol{D}\boldsymbol{f}\|^2 = \|\boldsymbol{v}\|^2$, the following cost function must be minimized:

$$\Psi(\boldsymbol{f}) = \boldsymbol{f}^t \log_2(\boldsymbol{f}) - \lambda \left[\|\boldsymbol{g} - \boldsymbol{D}\boldsymbol{f}\|^2 - \|\boldsymbol{v}\|^2 \right] \tag{59}$$

where λ is a Lagrangian multiplier.

Solving for $\hat{\boldsymbol{f}}$ leads to [17]:

$$\hat{\boldsymbol{f}} \cong (\boldsymbol{D}^{*t}\boldsymbol{D} + \eta \boldsymbol{I})^{-1} \boldsymbol{D}^{*t} \boldsymbol{g} \tag{60}$$

where $\eta = -1/(2\lambda \ln(2))$.

The inversion of the term $\boldsymbol{D}^{*t}\boldsymbol{D} + \eta\boldsymbol{I}$ can be performed easily depending of the special nature of this matrix, which is a sparse matrix. The effect of the term $\eta\boldsymbol{I}$ is to remove the ill posedness nature of the inverse problem by redistributing the eigen values of the term $\boldsymbol{D}^{*t}\boldsymbol{D}$ to avoid singularity.

3.5.3. Regularized Image Interpolation

Regularization theory was first introduced by Tikhonov and Miller. It provides a formal basis for the development of regularized solutions of ill posed problems [34–36]. The stabilizing function technique is one of the basic methodologies for the development of regularized solutions. According to this approach, an ill-posed problem can be regarded as the constrained minimization of a certain function, called the stabilizing function. The specific constraints imposed by the stabilizing function technique on the solution depend on the form and the properties of the stabilizing function used.

According to the regularization approach, the solution of Eq. (1) is obtained by the minimization of the following cost function [16, 17]:

$$\Psi(\boldsymbol{f}) = \|\boldsymbol{g} - \boldsymbol{D}\boldsymbol{f}\|^2 + \lambda\|\boldsymbol{C}\boldsymbol{f}\|^2 \tag{61}$$

where $\boldsymbol{C}$ is the regularization operator and λ is the regularization parameter.

This minimization is accomplished by taking the derivative of the cost function yielding:

$$\frac{\partial\Psi(\boldsymbol{f})}{\partial\boldsymbol{f}} = \boldsymbol{0} = 2\boldsymbol{D}^t(\boldsymbol{g} - \boldsymbol{D}\hat{\boldsymbol{f}}) - 2\lambda\boldsymbol{C}^t\boldsymbol{C}\hat{\boldsymbol{f}} \tag{62}$$

Solving for $\hat{\boldsymbol{f}}$ that provides the minimum of the cost function yields [16, 17]:

$$\hat{\boldsymbol{f}} = (\boldsymbol{D}^t\boldsymbol{D} + \lambda\boldsymbol{C}^t\boldsymbol{C})^{-1}\boldsymbol{D}^t\boldsymbol{g} \tag{63}$$

The solution of the regularized image interpolation problem can't be solved as a direct inversion process for the whole image due to the large computational complexity of the inversion process. One of the possible previously suggested solutions to this problem is to use successive approximation techniques for the solution.

In this section, we suggest another solution to the regularized image interpolation problem. This solution is implemented by the segmentation of the LR image into overlapping segments and interpolating each segment alone using Eq. (63) [16, 17]. It is clear that, if a global regularization parameter is used, a single matrix inversion process for a matrix of small dimensions is required because the term $(\boldsymbol{D}^t\boldsymbol{D} + \lambda\boldsymbol{C}^t\boldsymbol{C})^{-1}$ is independent on the image to be interpolated. Thus, the algorithm is efficient from the point of view of computation time.

The results of inverse image interpolation are given in Fig. 10 and Table 5. These results give the conclusion that inverse image interpolation is better than traditional image interpolation.

(a) LR Lenna image SNR=25 dB

(b) Bilinear interpolation

(c) LMMSE interpolation with autocorrelation estimated from bilinear interpolated image.

(c) Bicubic interpolation

(d) LMMSE interpolation with autocorrelation estimated from bicubic interpolated image.

(e) Maximum entropy image interpolation η=0.001.

(f)) Regularized image interpolation λ=0.001.

Figure 10. Inverse interpolation results.

4. SUPER-RESOLUTION RECONSTRUCTION OF IMAGES

The super resolution reconstruction problem is an ill-posed inverse problem having matrices of very large dimensions. This problem has been previously treated in the literature [18–29]. The first treatment to the supper resolution reconstruction problem was an iterative frequency domain treatment since the Fourier transform has superior properties for translational shifts between observations [18–20]. The maximum a posteriori (MAP) estimation algorithm has been implemented in the field of image super resolution [21–23]. Some other set theoretic approaches have also been presented

Table 5. MSE Interpolation results for different images with SNR = 25 dB. Column 3 of LMMSE interpolation uses the bilinear interpolation in estimating the HR image autocorrelation matrix. Column 5 of LMMSE interpolation uses the bicubic interpolation in estimating the HR image autocorrelation matrix.

Image	Bilinear Interpolation	LMMSE Interpolation	Bicubic Interpolation	LMMSE Interpolation	Maximum Entropy Interpolation η=0.001	Regularized Interpolation λ=0.001
Cameraman	256	215	248	224	199	151
Lenna	341	284	332	290	280	219
Mandrill	259	215	255	216	218	202
Building	1156	862	1167	869	840	958
TestPat1	342	235	313	242	296	6 9

[20–24]. The special nature of this problem forces most image super resolution reconstruction algorithms to have an iterative nature. These algorithms aim at reducing the computational cost of the matrix inversion processes involved in the solution by using successive approximation methods for the estimation of the HR image.

Most of the previously suggested solutions to this problem are based on the regularization theory [18–29]. The iterative implementation of the regularization theory in image super resolution has been the most popular procedure to solve the problem. Although these algorithms avoid matrix inversions, they are still time consuming and can't be implemented beyond a certain limit of dimensionality.

In this section, we suggest a general framework for image super resolution based on wavelet fusion. In this framework, we propose four non-iterative algorithms for image super resolution. These algorithms are LMMSE super resolution, maximum entropy super resolution, regularized super resolution and blind super resolution using wavelet fusion. The suggested algorithms are based on breaking the super resolution reconstruction problem into four consecutive steps to work on large dimension images. These steps are a registration step, a multi-channel restoration step, a wavelet-based image fusion and denoising step and an image interpolation step. The difference between the suggested algorithms is in the multi-channel restoration step and the interpolation step. The wavelet image fusion process is used in our suggested algorithms as a tool to integrate the information obtained from all the outputs of the multi-channel restoration step into a single image. The obtained image is then interpolated to give an HR image.

4.1. Multi-Channel LR Degradation Model

In super resolution image reconstruction algorithms, several degraded LR observations are used to estimate a single HR image. The mathematical model which relates the available LR observations to the required HR image is given by [18–33]:

$$\boldsymbol{g}_k = \boldsymbol{D}_k \boldsymbol{B}_k \boldsymbol{M}_k \boldsymbol{f}_h + \boldsymbol{v}_k \qquad 1 \le k \le P \tag{64}$$

where P is the number of available observations, $\boldsymbol{g}_k$ is an $(M^2 \times 1)$ vector representing the kth $(M \times M)$ LR image in lexicographic order. $\boldsymbol{f}_h$ is an $(N^2 \times 1)$ vector representing an $(N \times N)$ HR image in lexicographic order. $\boldsymbol{M}_k$ is the $(N^2 \times N^2)$ registration shift matrix and $\boldsymbol{B}_k$ is the blur matrix of size $(N^2 \times N^2)$. $\boldsymbol{D}_k$ is the $(M^2 \times N^2)$ uniform down sampling matrix. $\boldsymbol{v}_k$ is the $M^2 \times 1$ noise vector.

Equation (64) can be rewritten in the following form:

$$\begin{bmatrix} \boldsymbol{g}_1 \\ \vdots \\ \boldsymbol{g}_P \end{bmatrix} = \begin{bmatrix} \boldsymbol{D}_1 \boldsymbol{B}_1 \boldsymbol{M}_1 \\ \vdots \\ \boldsymbol{D}_p \boldsymbol{B}_p \boldsymbol{M}_p \end{bmatrix} \boldsymbol{f}_h + \begin{bmatrix} \boldsymbol{v}_1 \\ \vdots \\ \boldsymbol{v}_P \end{bmatrix} \tag{65}$$

Simplifying Eq. (65) leads to:

$$\boldsymbol{g} = \boldsymbol{L} \boldsymbol{f}_h + \boldsymbol{v} \tag{66}$$

where:

$$\boldsymbol{g} = \begin{bmatrix} \boldsymbol{g}_1 \\ \vdots \\ \boldsymbol{g}_P \end{bmatrix}, \quad \boldsymbol{L} = \begin{bmatrix} \boldsymbol{D}_1 \boldsymbol{B}_1 \boldsymbol{M}_1 \\ \vdots \\ \boldsymbol{D}_p \boldsymbol{B}_p \boldsymbol{M}_p \end{bmatrix}, \quad \boldsymbol{v} = \begin{bmatrix} \boldsymbol{v}_1 \\ \vdots \\ \boldsymbol{v}_P \end{bmatrix} \tag{67}$$

Using the regularization theory to solve Eq. (66), we get [76, 78, 83]:

$$\hat{\boldsymbol{f}}_h = [\boldsymbol{L}^t \boldsymbol{L} + \tau \boldsymbol{C}^t \boldsymbol{C}]^{-1} \boldsymbol{L}^t \boldsymbol{g} \tag{68}$$

where $\boldsymbol{C}$ is the regularization operator which is preferred to be the 3-D Laplacian operator to capture the between channel information in the reconstruction process. The parameter τ is a global regularization parameter.

There is a problem in the implementation of Eq. (68). The matrix inversion process can't be performed directly and no approximations, such as the Toplitz to circulant approximation, can be used to diagonalize the matrices involved in the inversion process. This is because L is not a square matrix. In the following section, we present a different treatment to this ill-posed problem, which removes these computational limitations.

4.2. Suggested Super Resolution Reconstruction Approach

In this section, we suggest a new approach to image super resolution based on wavelet fusion [30–33]. The implementation of this approach is composed of four consecutive steps. In the general solution of the super resolution reconstruction problem, we deal with three degradation phenomena, a general geometric registration warp, blurring and additive noise. Based on these phenomena, we can break the solution into the following consecutive steps.

Step 1: Image alignment, which means estimating the geometrical registration warp between different images.

Step 2: Multi-channel image restoration of the registered degraded observations.

Step 3: Wavelet based fusion of the multiple images obtained from step 2 to form a single image.

Step 4: Image interpolation of the resulting image from step 3 to obtain an HR image.

4.3. Simplified Multi-Channel Degradation Model

The multi channel image restoration step aims at obtaining multiple undegraded images of the same dimensions as that of the available LR images. These obtained images are then used in the next step of image fusion. This step requires that a simplified degradation model is used. This model doesn't consider the operator D of filtering and down sampling. For a multi channel imaging system with P channels each of size $M \times M$, the simplified degradation model becomes [30–32]:

$$\boldsymbol{g}_k = \boldsymbol{B}_k \boldsymbol{M}_k \boldsymbol{f}_k + \boldsymbol{v}_k \qquad \text{for } k = 1, 2, , \ldots, P \tag{69}$$

where $\boldsymbol{g}_k, \boldsymbol{f}_k$ and $\boldsymbol{v}_k$ are the observed image, the ideal image and the noise of the kth channel, respectively. $\boldsymbol{B}_k$ is the degradation matrix of the kth channel. $\boldsymbol{M}_k$ is the relative registration shift operator of the kth channel. In this paper, we restrict our work to global translational shifts, which is the case of consideration in most image super resolution reconstruction algorithms. Translational motion can be approximated by circular motion except near edge pixels [30–32]. Using this approximation, the matrices $\boldsymbol{M}_k$ can be approximated by circulant matrices for all values of k.

Equation (69) can be written in the following form:

$$\boldsymbol{g} = \boldsymbol{B}\boldsymbol{M}\boldsymbol{f} + \boldsymbol{v} \tag{70}$$

where

$$\boldsymbol{g} = \begin{bmatrix} \boldsymbol{g}_1 \\ \boldsymbol{g}_2 \\ \vdots \\ \boldsymbol{g}_P \end{bmatrix};\ \boldsymbol{f} = \begin{bmatrix} \boldsymbol{f}_1 \\ \boldsymbol{f}_2 \\ \vdots \\ \boldsymbol{f}_P \end{bmatrix};\ \boldsymbol{v} = \begin{bmatrix} \boldsymbol{v}_1 \\ \boldsymbol{v}_2 \\ \vdots \\ \boldsymbol{v}_P \end{bmatrix};\ \boldsymbol{B} = \begin{bmatrix} \boldsymbol{B}_1 & \boldsymbol{0} & \cdots & \boldsymbol{0} \\ \boldsymbol{0} & \boldsymbol{B}_2 & \cdots & \boldsymbol{0} \\ \vdots & \vdots & \cdots & \vdots \\ \boldsymbol{0} & \boldsymbol{0} & \cdots & \boldsymbol{B}_P \end{bmatrix}$$

and

$$\boldsymbol{M} = \begin{bmatrix} \boldsymbol{M}_1 & \boldsymbol{0} & \cdots & \boldsymbol{0} \\ \boldsymbol{0} & \boldsymbol{M}_2 & \cdots & \boldsymbol{0} \\ \vdots & \vdots & \cdots & \vdots \\ \boldsymbol{0} & \boldsymbol{0} & \cdots & \boldsymbol{M}_P \end{bmatrix} \tag{71}$$

If we define:

$$\boldsymbol{H} = \boldsymbol{B}\boldsymbol{M} \tag{72}$$

Then, the multi-channel image degradation model can be written in the form [30–32]:

$$\boldsymbol{g} = \boldsymbol{H}\boldsymbol{f} + \boldsymbol{v} \tag{73}$$

where $\boldsymbol{g}$, $\boldsymbol{f}$ and $\boldsymbol{v}$ are $P \times M^2$ in length. The degradation operator $\boldsymbol{H}$ of the multi channel-imaging model is of dimensions $(P \times M^2) \times (P \times M^2)$. We can assume $\boldsymbol{f}_1 = \boldsymbol{f}_2 = \cdots = \boldsymbol{f}_P$.

According to the model given in Eq. (73), the multi-channel rstoration process is similar to that of the inverse image interpolation process but with $\boldsymbol{D}$ replaced by $\boldsymbol{H}$. Thus, the same techniques used for inverse image interpolation are applicable for multi-channel restoration but with different implementation methods [30–34].

4.4. Multi Channel Image Restoration

4.4.1. Multi-Channel LMMSE Restoration

The LMMSE solution to the multi-channel image restoration problem is, thus, given by [30]:

$$\hat{\boldsymbol{f}} = \boldsymbol{R}_f \boldsymbol{H}^t [\boldsymbol{H}\boldsymbol{R}_f \boldsymbol{H}^t + \boldsymbol{R}_v]^{-1} \boldsymbol{g} \tag{74}$$

4.4.2. Multi-Channel Maximum Entropy Restoration

Using the concept of entropy maximization, the solution of the simplified multi-channel image degradation model is represented as follows [31]:

$$\hat{\boldsymbol{f}} \cong (\boldsymbol{H}^t \boldsymbol{H} + \eta \boldsymbol{I})^{-1} \boldsymbol{H}^t \boldsymbol{g} \tag{75}$$

4.4.3. Multi-Channel Regularized Restoration

Solving for $\hat{\boldsymbol{f}}$ using the regularization concept gives [32]:

$$\hat{\boldsymbol{f}} = [\boldsymbol{H}^t\boldsymbol{H} + \boldsymbol{\Lambda}^{-1}\boldsymbol{C}^t\boldsymbol{C}]^{-1}\boldsymbol{H}^t\boldsymbol{g} \tag{76}$$

where $\boldsymbol{\Lambda}$ is defined by:

$$\boldsymbol{\Lambda} = \begin{bmatrix} \lambda_1[\boldsymbol{I}] & \mathbf{0} & \cdots & \mathbf{0} \\ \mathbf{0} & \lambda_2[\boldsymbol{I}] & \cdots & \mathbf{0} \\ \vdots & \vdots & \cdots & \vdots \\ \mathbf{0} & \mathbf{0} & \cdots & \lambda_P[\boldsymbol{I}] \end{bmatrix} \tag{77}$$

The identity matrix $\boldsymbol{I}$ is of size $M^2 \times M^2$.

The suggested super resolution image reconstruction algorithms are tested on different noisy LR degraded observations with different signal to noise ratios. Several experiments have been conducted in this test. In the first experiment, three LR degraded observations of Lenna image of size 128×128 are used to obtain a single HR image of size 256×256. The general degradation model of Eq. (64) is used to generate the degraded observations. The degradation in each observation comprises a relative translational shift with the reference observation, an out of focus blurring and additive noise with $SNR = 40\,\text{dB}$. The original LR image is shown in Fig. 11. The degraded observations are given in Fig. 12.

Figure 11. Original Lenna image.

The LMMSE interpolated version of the original LR image is given in Fig. 13. The image obtained from the fusion of the outputs of the multi-channel LMMSE restoration step is given in Fig. 14a. The HR image obtained using the LMMSE super resolution algorithm is given in Fig. 14b. It is clear that the computation time is moderate but the visual quality and the PSNR value obtained are not satisfactory.

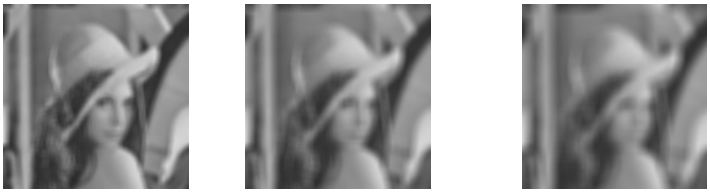

(a) observation (1) 5×5 Blur operator

(b) observation (2) 7×7 Blur operator

(c) observation (3) 9×9 Blur operator

Figure 12. Available observations $SNR = 40\,\text{dB}$.

Figure 13. LMMSE interpolation of the original image.

(a) Fused Image PSNR=24.3 dB

(b) LMMSE interpolation of the fused image PSNR=24.2 dB

Figure 14. Results of the LMMSE Super-resolution reconstruction algorithm. CPU = 55 sec.

Figure 15. Maximum entropy interpolation of the original image.

(a) Fused Image
PSNR=26.43 dB

(b) Obtained HR image
PSNR=26.47 dB
CPU=10 sec on a 1
GHz Processor

Figure 16. Results of the maximum entropy super resolution reconstruction algorithm.

The maximum entropy interpolated version of the original LR image is given in Fig. 15. The image obtained from the fusion of the outputs of multi-channel maximum entropy restoration step is given in Fig. 16a. The HR image obtained using the maximum entropy super resolution algorithm is given in Fig. 16b. The parameter η used in the multi channel restoration step and in the interpolation step is 0.001. It is clear from the obtained results that the computation time is reduced significantly and the visual quality and the PSNR value obtained get better.

The regularized interpolated version of the original LR image is given in Fig. 17. The image obtained from the fusion of the outputs

Figure 17. Regularized interpolation of the original image.

(a) Fused Image
PSNR=27.7 dB

(b) Obtained HR image
PSNR=27.7 dB
CPU=105 sec on a 1
GHz Processor

Figure 18. Results of the regularized super-resolution reconstruction algorithm.

of multi-channel regularized restoration step is given in Fig. 18a. The HR image obtained using the regularized super resolution algorithm is given in Fig. 18b. The optimum values of the Lagrangian multipliers used in the multi-channel regularized restoration step are estimated using Newton method. The parameter λ used in the interpolation step is 0.001. It is clear from the obtained results that the PSNR value obtained using this algorithm is the highest obtained value but at the cost of much more computation time.

The fusion rule used in all algorithms is the maximum frequency rule. The wavelet fusion process is performed in one decomposition level using the Haar basis function. The PSNR values given in part (a)

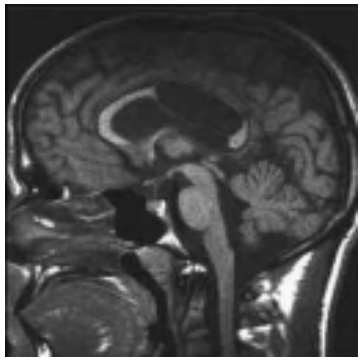

Figure 19. Original MRI image.

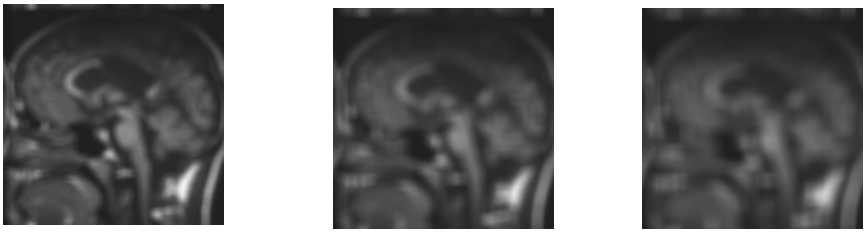

(a) observation (1) 5×5 Blur operator

(b) observation (2) 7×7 Blur operator

(c) observation (3) 9×9 Blur operator

Figure 20. Available observations $SNR = 40\,\text{dB}$.

of Figs. 14, 16 and 18 are calculated using the MSE between the fused image and the original LR image given in Fig. 11. On the other hand, the PSNR values given in part (b) of the same figures are calculated using the MSE between the obtained HR image and the interpolated version of the original LR image using the same algorithm used to obtain the HR image.

Other experiments on an MRI image has been carried out to test the suggested algorithms. The results of these experiments are given in Figs. 19 to 26. The PSNR values are estimated as in the first experiment.

The experiments carried out in this section using the suggested super resolution reconstruction algorithms are very difficult to be implemented using the traditional iterative solutions due to the very large dimension matrices required which can't be saved using traditional PCs as mentioned previously. It is clear that the suggested

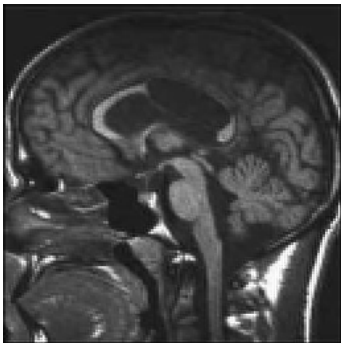

Figure 21. LMMSE interpolation of the original image.

(a) Fused Image
PSNR=18.85 dB

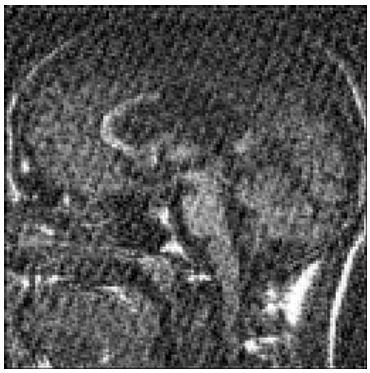

(c) LMMSE interpolation of the fused image
PSNR=18.66 dB

Figure 22. Results of the LMMSE Super-resolution reconstruction algorithm. CPU = 55 sec.

algorithms have succeeded in obtaining HR images with good visual quality as compared to the available observations and high PSNR values. The computation cost is acceptable when the quality of the HR image obtained is the most important factor. Regularized super resolution is the best algorithm from the visual quality point of view but it has the maximum computation time. The success of the suggested algorithms with three observations only is an indication of the superiority of these algorithms to the previously mentioned algorithms which require a large number of frames to obtain a single HR image.

Figure 23. Maximum entropy interpolation of the original image.

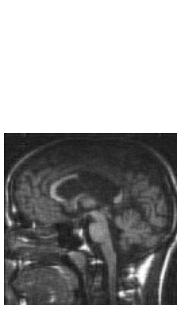

(a) Fused Image
PSNR=28.71 dB

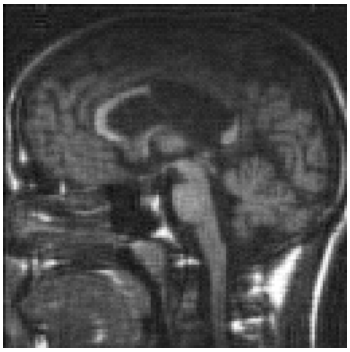

(b) Obtained HR image
PSNR=28.74 dB
CPU=105 sec on a 1
GHz Processor

Figure 24. Results of the maximum entropy super resolution reconstruction algorithm.

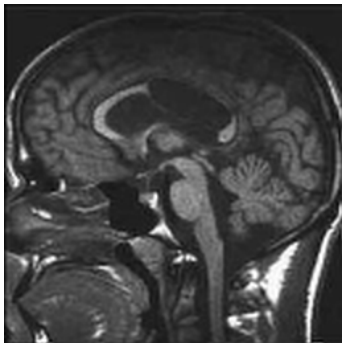

Figure 25. Regularized interpolation of the original image.

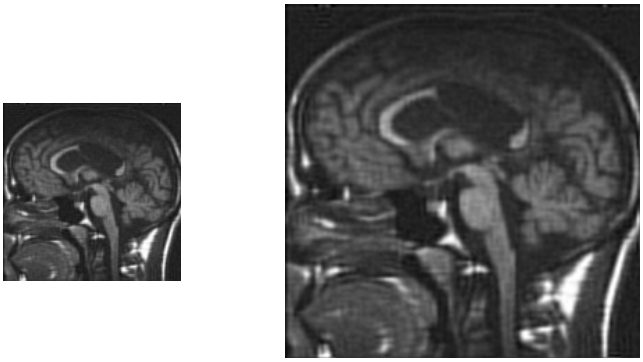

(a) Fused Image PSNR=32.44 dB

(b) Obtained HR image PSNR=31.49 dB CPU=105 sec on a 1 GHz Processor

Figure 26. Results of the regularized super resolution reconstruction algorithm.

4.4.4. Blind Super Resolution Reconstruction Approach

Assume that we have K degraded observations of the same scene given by the following equation [33, 34]:

$$g_k(m,n) = f(m,n)^* b_k(m,n) + v_k(m,n),\ k = 1, 2, \ldots, K \tag{78}$$

To incorporate the information in each observation into the restoration process, we suggest generating a new observation image represented by the following equation [33, 34]:

$$g_{K+1}(m,n) = \sum_{k=1}^{K} w_k g_k(m,n) \tag{79}$$

where w_k values are scalars chosen according to the estimation of the SNR in each image which is made using the noise variance estimations. Another restriction on the values of w_k is the normalization condition as follows [33, 34]:

$$\sum_{k=1}^{K} w_k = 1 \tag{80}$$

Substituting from Eq. (79) into Eq. (78), we get:

$$g_{K+1}(m,n) = \sum_{k=1}^{K} w_k [f(m,n)^* b_k(m,n) + v_k(m,n)] \tag{81}$$

Thus:

$$g_{K+1}(m,n) = f(m,n)^* \left[\sum_{k=1}^{K} w_k b_k(m,n)\right] + \sum_{k=1}^{K} w_k v_k(m,n) \tag{82}$$

This equation can be written in the form [33, 34]:

$$g_{K+1}(m,n) = f(m,n)^* b_{K+1}(m,n) + v_{K+1}(m,n) \tag{83}$$

where

$$b_{K+1}(m,n) = \left[\sum_{k=1}^{K} w_k b_k(m,n)\right] \tag{84}$$

and

$$v_{K+1}(m,n) = \sum_{k=1}^{K} w_k v_k(m,n) \tag{85}$$

It can be proved that in z-domain, $B_{K+1}(z_1, z_2)$ is co-prime with all B_ks if each $B_k(z_1, z_2)$ is co-prime with all other B_ks for $k \leq K$ [33, 34].

Thus, the 2-D GCD algorithm can be carried out between the z-transforms of $g_{K+1}(m,n)$ and any of $g_k(m,n)$ where $k \leq K$ to give good estimates of $F(z_1, z_2)$ and hence $f(m,n)$.

The relation $v_{K+1}(m,n) = \sum_{k=1}^{K} w_k v_k(m,n)$ leads to an image with noise variance σ^2_{K+1} given by:

$$\sigma^2_{K+1} = \sum_{k=1}^{K} w_k^2 \sigma_k^2. \tag{86}$$

For equal weight averaging, we have $w_1 = w_2 = \cdots = w_K = 1/K$. Thus:

$$\sigma^2_{K+1} = \sum_{k=1}^{K} \frac{\sigma_k^2}{K^2} \tag{87}$$

The assumption that all observations are taken in the same noisy environment leads to [97, 98]:

$$\sigma^2_{K+1} = \frac{\sigma_k^2}{K} \tag{88}$$

The above equation leads to an improvement of the SNR in the image $g_{K+1}(m,n)$ by a factor of K. This increase in SNR enables a robust application of the 2-D GCD algorithm between $g_{K+1}(m,n)$ and any other observation $g_k(m,n)$ in the z-domain since this 2-D GCD algorithm is very sensitive to the presence of noise.

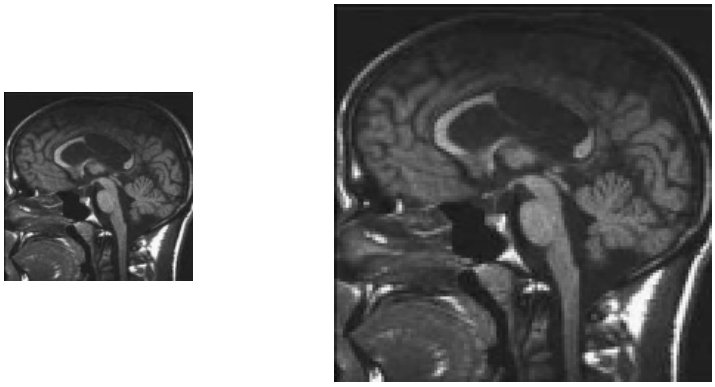

(a) Original image

(b) Maximum Entropy interpolation of the original image

Figure 27. Original undegraded MRI image.

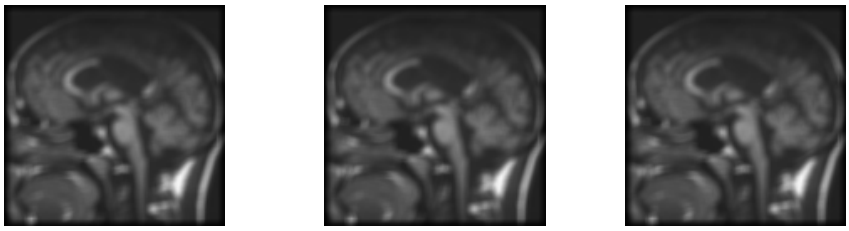

(a) observation (1) (b) observation (2) (c) observation (3)

Figure 28. Available observations 5×5 blur operator $SNR = 60\,\text{dB}$.

The suggested blind super resolution image reconstruction approach is tested using three degraded observations of the same MRI image blurred with different co-prime blurring operators. Each observation is of size (128×128) pixels and the signal to noise ratio in each observation is 60 dB. The original image and its maximum entropy interpolated version are given in Fig. 27. The degraded observations are given in Fig. 28. A combinational image is generated from the available degraded observations by equal weight averaging. The GCD is estimated between the obtained combinational image and each one of the available observations. The multiple outputs obtained from this step are fused on a wavelet basis. The image obtained from the wavelet based fusion step is given in Fig. 29a. The rule used in image fusion is the maximum frequency rule and the fusion process is

(b) Fused Image

(c) Obtained HR image
PSNR=30.2 dB
CPU=55 sec on a 1
GHz Processor

Figure 29. Results of the blind super resolution reconstruction algorithm.

performed in one decomposition level. Applying the maximum entropy image interpolation algorithm on that image in Fig. 29a gives the HR image in Fig. 29b. It is clear that the suggested blind super resolution reconstruction algorithm has succeeded in obtaining an HR image with a good visual quality and a high PSNR in a small time.

5. CONCLUSIONS

This paper reveals the importance of the branch of image processing called HR image processing. The two main topics that are of great importance in HR image processing are studied. Existing as well as suggested new techniques in HR image processing are compared from the MSE or PSNR and the computational complexity points of view. The paper should motivate the work in the field of HR image processing towards more efficient image interpolation and super resolution approaches.

REFERENCES

1. Unser, M., A. Aldroubi, and M. Eden, "B-spline signal processing: Part I-Theory," *IEEE Trans. Signal Processing*, Vol. 41 No. 2, 821–833, Feb. 1993.
2. Unser, M., A. Aldroubi, and M. Eden, "B-spline signal processing:

Part II-Efficient design and applications," *IEEE Trans. Signal Processing*, Vol. 41, No. 2, 834–848, Feb. 1993.

3. Unser, M., "Splines a perfect fit for signal and image processing," *IEEE Signal Processing Magazine*, November 1999.
4. Hou, H. S. and H. C. Andrews, "Cubic spline for image interpolation and digital filtering," *IEEE Trans. Accoustics, Speech and Signal Processing*, Vol. ASSP-26, No. 9, 508–517, December 1978.
5. Thevenaz, P., T. Blu, and M. Unser, "Interpolation revisited," *IEEE Trans. Medical Imaging*, Vol. 19, No. 7, 739–758, July 2000.
6. Blu, T., P. Thevenaz, and M. Unser, "MOMS: Maximal-order interpolation of minimal support," *IEEE Trans. Image Processing*, Vol. 10, No. 7, 1069–1080, 2001.
7. Vrcelj, B. and P. P. Vaidyanathan, "Efficient implementation of all digital interpolation," *IEEE Trans. Image Processing*, Vol. 10, No. 11, 1639–1646, November 2001.
8. Han, J. K. and H.-M. Kim, "Modified cubic convolution scaler with minimum loss of information," *Optical Engineering*, Vol. 40, No. 4, 540–546, April 2001.
9. Ramponi, G., "Warped distance for space variant linear image interpolation," *IEEE Trans. Image Processing*, Vol. 8, 629–639, 1999.
10. El-Khamy, S. E., M. M. Hadhoud, M. I. Dessouky, B. M. Salam, and F. E. A. El-Samie, "A simple adaptive interpolation approach based on varying image local activity levels," *International Journal of Information Acquisition*, Vol. 3, No. 1, World-Science Inc., March 2006.
11. El-Khamy, S. E., M. M. Hadhoud, M. I. Dessouky, B. M. Salam, and F. E. A. El-Samie, "An adaptive cubic convolution image interpolation approach," *International Journal of Machine Graphics & Vision*, Vol. 14, No. 3, 235–256, 2005.
12. El-Khamy, S. E., M. M. Hadhoud, M. I. Dessouky, B. M. Salam, and F. E. Abd El-Samie, "A new approach for adaptive polynomial based image interpolation," *International Journal of Information Acquisition*, Vol. 3, No. 2, 139–159, World-Science Inc., 2006.
13. Leung, W. Y. V. and P. J. Bones, "Statistical interpolation of sampled images," *Opt. Eng.*, Vol. 40, No. 4, 547–553, April 2001.
14. Shin, J. H., J. H. Jung, and J. K. Paik, "Regularized iterative image interpolation and its application to spatially scalable coding," *IEEE Trans. Consumer Electronics*, Vol. 44, No. 3, 1042–

1047, August 1998.

15. El-Khamy, S. E., M. M. Hadhoud, M. I. Dessouky, B. M. Salam, and F. E. A. El-Samie, "Optimization of image interpolation as an inverse problem using the LMMSE algorithm," *Proceedings of the IEEE MELECON*, 247–250, Croatia, May 2004.
16. El-Khamy, S. E., M. M. Hadhoud, M. I. Dessouky, B. M. Salam, and F. E. A. El-Samie, "A new approach for regularized image interpolation," *Journal of The Brazilian Computer Society*, Vol. 11, No. 3, April 2006.
17. El-Khamy, S. E., M. M. Hadhoud, M. I. Dessouky, B. M. Sallam, and F. E. A. El-Samie, "Efficient implementation of image interpolation as an inverse problem," *Journal of Digital Signal Processing*, Vol. 15, No. 2, 137–152, Elsevier Inc., March 2005.
18. Kim, S. P. and W. Y. Su, "Recursive high resolution reconstruction of blurred multiframe images," *IEEE Trans. Image Processing*, Vol. 2, No. 4, 534–539, October 1993.
19. Kim, S. P., N. K. Bose, and H. M. Valenzuela, "Recursive reconstruction of high resolution image from noisy undersampled multiframes," *IEEE Trans. Acoustics, Speech and Signal Processing*, Vol. 38, No. 6, 1013–1027, June 1990.
20. Park, S. C., M. K. Park, and M. G. Kang, "Super-resolution image reconstruction: A technical overview," *IEEE Signal Processing Magazine*, Vol. 20, No. 3, 21–36, May 2003.
21. Eren, P. E., M. I. Sezan, and M. Tekalp, "Robust, object based high resolution image reconstruction from low resolution vedio," *IEEE Trans. Image Processing*, Vol. 6, No. 10, 1446–1451, October 1997.
22. Elad, M. and A. Feuer, "Restoration of a single superresolution image from several blurred, noisy, and undersampled measured images," *IEEE Trans. Image Processing*, Vol. 6, No. 12, 1646–1658, December 1997.
23. Capel, D. and A. Zisserman, "Computer vision applied to super-resolution," *IEEE Signal Processing Magazine*, Vol. 20, No. 3, 75–86, May 2003.
24. Nguyen, N., P. Milanfar, and G. Golub, "A computationally efficient superresolution image reconstruction algorithm," *IEEE Trans. Image Processing*, Vol. 10, No. 4, 573–583, April 2001.
25. Rajan, D., S. Chandhuri, and M. V. Joshi, "Multi-objective super-resolution: Concepts and examples," *IEEE Signal Processing Magazine*, Vol. 20, No. 3, 49–61, May 2003.
26. Segall, C. A., R. Molina, and A. K. Katsaggelos, "High-resolution

images from low-resolution compressed video," *IEEE Signal Processing Magazine*, Vol. 20, No. 3, 37–48, May 2003.

27. Elad, M. and A. Feuer, "Super-resolution restoration of an image sequence: Adaptive filtering approach," *IEEE Trans. Image Processing*, Vol. 8, No. 3, 387–395, March 1999.
28. Ng, M. K. and N. K. Bose, "Mathematical analysis of super-resolution methodology," *IEEE Signal Processing Magazine*, Vol. 20, No. 3, 62–74, May 2003.
29. Vega, M., J. Mateos, R. Molina, and A. K. Katsagegelos, "Bayesian parameter estimation in image reconstruction from subsampled blurred observations," *Proc. of ICIP 2003*.
30. El-Khamy, S. E., M. M. Hadhoud, M. I. Dessouky, B. M. Salam, and F. E. Abd El-Samie, "Wavelet fusion: A tool to break the limits on LMMSE image super-resolution," *International Journal of Wavelets, Multiresolution and Information Processing IJWMIP*, Vol. 4, No. 1, World Science Inc., March 2006.
31. El-Khamy, S. E., M. M. Hadhoud, M. I. Dessouky, B. M. Salam, and F. E. Abd El-Samie, "A wavelet based entroptic approach to high-resolution image reconstruction," Accepted for publication in *International Journal of Machine Graphics and Vision*.
32. El-Khamy, S. E., M. M. Hadhoud, M. I. Dessouky, B. M. Salam, and F. E. A. El-Samie, "Regularized super-resolution reconstruction of images using wavelet fusion," *Journal of Optical Engineering*, Vol. 44, No. 9, September 2005.
33. El-Khamy, S. E., M. M. Hadhoud, M. I. Dessouky, B. M. Salam, and F. E. A. El-Samie, "Blind reconstruction of high resolution images using wavelet fusion," *Journal of Applied Optics*, Vol. 44, No. 34, Optical Society of America (OSA), December 2005.
34. El-Khamy, S. E., M. M. Hadhoud, M. I. Dessouky, B. M. Salam, and F. E. Abd El-Samie, "A GCD approach to blind super-resolution reconstruction of images," *Journal of Modern Optics*, Vol. 53, No. 8, May 2006.